How pore formation in complex biological membranes is governed by lipid composition, mechanics, and lateral sorting

Leonhard J. Starke [ID][a], Christoph Allolio[b] and Jochen S. Hub [ID][a,*]

[a]Theoretical Physics and Center for Biophysics, Saarland University, 66123 Saarbrücken, Germany
[b]Faculty of Mathematics and Physics, Charles University, 121 16 Prague, Czech Republic
*To whom correspondence should be addressed: Email: jochen.hub@uni-saarland.de
Edited By Gerhard Hummer

Abstract

The primary function of biological membranes is to enable compartmentalization among cells and organelles. Loss of integrity by the formation of membrane pores would trigger uncontrolled depolarization or influx of toxic compounds, posing a fatal threat to living cells. How the lipid complexity of biological membranes enables mechanical stability against pore formation while, simultaneously, allowing for ongoing membrane remodeling is largely enigmatic. We performed molecular dynamics simulations of eight complex lipid membranes including the plasma membrane and membranes of the organelles endoplasmic reticulum, Golgi, lysosome, and mitochondrion. To quantify the mechanical stability of these membranes, we computed the free energy of transmembrane pore nucleation as well as the line tension of the rim of open pores. Our simulations reveal that complex biological membranes are remarkably stable, however, with the plasma membrane standing out as exceptionally stable, which aligns with its crucial role as a protective layer. We observe that sterol content is a key regulator for biomembrane stability, and that lateral sorting among lipid mixtures influences the energetics of membrane pores. A comparison of 25 model membranes with varying sterol content, tail length, tail saturation, and head group type shows that the pore nucleation free energy is mostly associated with the lipid tilt modulus, whereas the line tension along the pore rim is determined by the lipid intrinsic curvature. Together, our study provides an atomistic and energetic view on the role of lipid complexity in biomembrane stability.

Keywords: lipid membranes, pore formation, molecular dynamics simulations, Helfrich theory

Significance Statement

Biomembranes have evolved to fulfill seemingly conflicting requirements. Membranes form a protective layer against bacterial or viral infection and against external mechanical, osmotic and toxic stress, thus requiring mechanical stability. Membranes are furthermore involved in ongoing remodeling for homeostasis, signaling, trafficking, and morphogenesis, necessitating a high degree of plasticity. How the chemical diversity of membranes, comprising hundreds of lipid species, contributes to enable both stability and plasticity is not well understood. We used molecular simulations and free energy calculations of pore formation in complex biomembranes to reveal how mechanical and geometric properties of lipids as well as lateral lipid sorting control the integrity of complex membranes.

Introduction

Biological membranes contain hundreds of distinct lipid species (1), which vary in their head group composition as well as in the length, unsaturation degree, and number of acyl chains (2). In addition to glycerophospholipids, which are the most abundant lipids in eukaryotes (2), membranes contain lipid classes such as sphingolipids, sterols, or single-tailed lipids. Lipid compositions vary not only between different species and cell types but furthermore between cellular organelles. For instance, the sterol content of eukaryotic membranes increases along the secretory pathway and is maximized in the plasma membrane (2). The complexity of many membranes is furthermore increased by asymmetric distributions of lipids between the two membrane leaflets (3, 4). The

biological functions and advantages of this chemical diversity are still largely enigmatic.

Biological membranes have evolved to fulfill seemingly conflicting mechanical requirements. On the one hand, membranes are subject to ongoing remodeling during cell division, endo- and exocytosis, or intracellular trafficking, thus requiring a high degree of structural plasticity. On the other hand, biological membranes serve as barriers between cells and their environment and, in eukaryotic cells, between organelles and the cytosol, thus requiring mechanical stability. Such stability is crucial to withstand the formation of undesired membrane pores, which would lead to potentially fatal transmembrane flux of polar solutes and loss of homeostasis. To realize how lipid complexity contributes to

reconcile such seemingly conflicting needs—plasticity and stability—it is mandatory to understand how lipid composition and spatial distribution control the free energy landscape of membrane remodeling.

To quantify membrane stability, we here focus on the resistance of membranes against transmembrane pore formation. Membrane pores may form under various biological or experimental conditions. Pores are formed by proteins such as bacterial toxins (5), antimicrobial peptides (6), or by proteins of the apoptotic machinery (7). Pores may be induced mechanically through high osmotic pressure (8) or by extensive tension in mechanically active tissue (9). During electroporation, pores are formed by external electric fields, as widely used in medicine and biotechnology to deliver bioactive substances into living cells or to kill malignant cells that are not accessible to surgery (10, 11). Recently, it was found that binding of divalent cations to anionic lipids may impose transmembrane potentials and, thereby, trigger pore formation and transmembrane ionic flux (12, 13).

Direct experimental observation of protein-free pores has been limited to large, micron-sized pores (8) while nanoscopic pores have been detected indirectly by measuring the permeation of ionic or photoactive compounds (14). Thus, molecular dynamics (MD) simulations have been used extensively to obtain structural and energetic insight into nanoscopic pores (15). According to MD simulations, pore nucleation evolves from local membrane thinning via the formation of a thin membrane-spanning water wire towards the formation of a toroidally shaped, nanometer-sized, hydrophilic transmembrane pore, characterized by tilted lipid arrangements along the pore rim (15–17). In absence of external stressors, pore formation involves considerable energetic costs owing to the initial water penetration into the hydrophobic membrane core as well as owing to membrane bending and lipid tilting deformations along the pore rim (15, 16, 18–21). Previous experimental and computational studies highlighted the effects of membrane thickness (22, 23) and cholesterol content (24, 25) on increased membrane stability against pore formation. On the contrary, the addition of anionic 16:0–18:1-phosphatidylglycerol (POPG) into 16:0–18:1-phospatidylcholine (POPC) membranes has been shown to reduce resistance against pore formation (26).

Previous MD studies of pore formation mostly focused on single-component membranes (22, 27–32) or on membranes with at most three to four molecular species (33). Only recently, coarse-grained simulations of electroporation in complex plasma membrane models were reported. In these simulations, pores formed predominantly in regions with enriched density of unsaturated lipid tails (34). However, since atomic details such as the hydrogen bond network of transmembrane water wires likely influence the free energy landscape of pore formation, all-atom simulations are required to obtain a quantitative understanding of pore formation in complex membranes.

Here, we used all-atom MD simulations to compute the free energy landscape of pore formation in complex models of eight different biological membranes including an asymmetric plasma membrane model (35), models of several cellular organelles (36, 37), and a membrane representing *Escherichia coli* polar lipid extract used previously in biophysical experiments (38). We computed potentials of mean force (PMFs) of pore nucleation and pore expansion to obtain two principal energetic parameters that quantify the membrane stability against defect formation: the pore nucleation free energy and the line tension along the pore rim (39, 40). The PMFs reveal that the plasma membrane—in particular its outer leaflet—is by far more stable against pore formation compared to membranes of intracellular compartments. To rationalize the wide range of membrane stabilities and to clarify how lipid species, lipid properties, and membrane elastic properties influence pore formation, we computed additional PMFs of pore formation for a large set of one- or two-component model membranes as well as membrane deformation energies in the context of the Helfrich–Kozlov–Hamm (HKH) (41, 42) continuum theory. We find that pore nucleation is primarily associated with lipid tilting energies, whereas the line tension along the pore is controlled by bending energies. Together, our calculations provide a comprehensive view on energetics, structures, and mechanisms of pore formation in biological and model membranes.

Results

We selected a set of eight membrane systems with complex lipid composition, which together represent a wide range of biologically relevant membranes. The complex model membranes include asymmetric models of a plasma membrane (43), the mitochondrial outer and inner membranes (36), as well as symmetric models with lipid composition from endosomes, lysosome, endoplasmic reticulum (ER), Golgi apparatus, and *E. coli* lipid extract (38). As shown in Fig. 1a, the lipid composition greatly varies among these membranes (see also Tables S2–S9). The *E. coli* lipid extract does not contain PC but is mostly composed of phosphatidylethanolamine (PE), phosphatidyl-glycerol (PG), and cardiolipin (CL) (44). Among the eukaryotic membranes, the sterol content increases along the secretory pathway with a low abundance in the ER and Golgi membranes, increased abundance in the lysosome and high abundance up to 54% in the outer leaflet plasma membrane. Besides cholesterol, which exhibits a strong preference for the outer plasma membrane leaflet (43), various other lipids are also distributed asymmetrically between the inner and the outer leaflet. Phosphatidylserine (PS) and PE lipids are enriched in the inner plasma membrane leaflet whereas sphingomyelin (SM) is enriched in the outer plasma membrane leaflet (Fig. 1a, leftmost column). Likewise, the mitochondrial membrane models are asymmetric, with phosphatidylinositol (PI) being enriched in the inner leaflet of the mitochondrial outer membrane and with CL being enriched in the inner leaflet of the mitochondrial inner membrane, where CL plays a role in stabilizing cristae shaped with negative curvature (45). Additional examples for organelle-specific enrichment of low-abundance lipid species are the presence of phosphatidic acid (PA) and diacylglycerol (DAG) in the ER membrane, rationalized by the function of the ER as the main site of lipid synthesis (2). However, the lipid compositions of different membranes reflect not only biochemical processes but furthermore the need to withstand different degrees of mechanical stress, likely rationalizing why the plasma membrane is thicker as compared to organelle membrane, as illustrated by the MD simulation snapshots of Fig. 1b/c.

Pore nucleation free energy ΔG_{nuc} and the line tension γ along the pore rim

To obtain quantitative and mechanistic insight into pore formation in complex membranes, we computed potentials of mean force (PMFs, also referred to as free energy profiles) of pore formation. PMFs were computed along a joint reaction coordinate ξ_{p} of pore nucleation and expansion (see Supplementary material) (39, 40). For $\xi_{\mathrm{p}} \lesssim 1$, the coordinate quantifies the degree of connectivity of a polar transmembrane defect (Fig. 2b–d) (40); for $\xi_{\mathrm{p}} \gtrsim 1$, the reaction coordinate quantifies the pore radius R in units
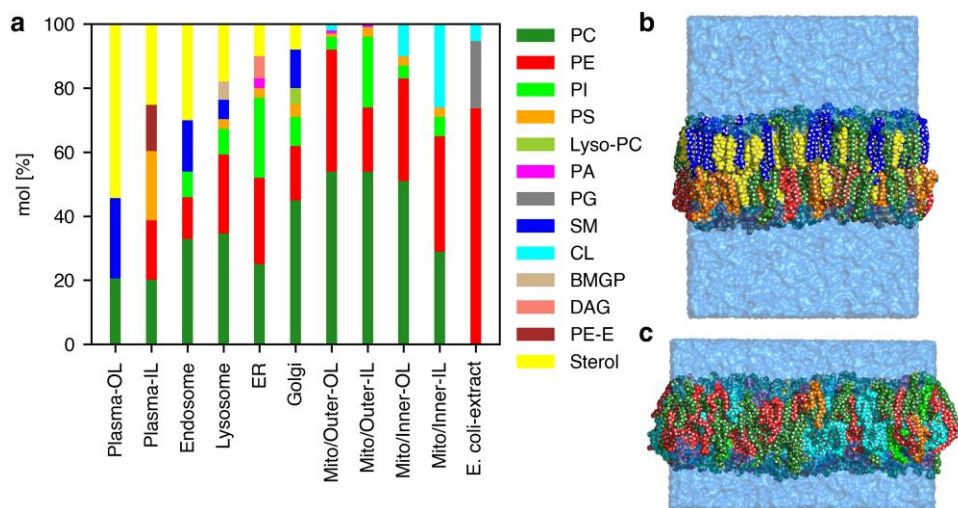
Fig. 1. Lipid head group composition of complex membrane systems. a) Composition of simulated biological membrane systems based on lipid species. PC, phosphatidyl-choline; PE, phosphatidyl-ethanolamine; PE-E, ether PE (plasmalogen); PI, phosphatidyl-inositol; PS, phosphatidyl-serine; PA, phosphatidic acid; PG, phosphatidylglycerol; SM, sphingomyelin; CL, cardiolipin, sterol (cholesterol for mammalian membranes, ergosterol for yeast ER); BMGP, bis(monoacylglycero)phosphate; DAG, diaglycerol, Lyso-PC: lyso-16:0-PC. For asymmetric models of the plasma membrane, mitochondrial outer (Mito/Outer) and inner membranes (Mito/Inner), the composition of the outer leaflet (OL) and the inner leaflet (IL) are shown. b) Simulation snapshot of the asymmetric plasma membrane and c) of the asymmetric inner mitochondrial membrane with lipid atoms shown as beads and colored according to the legend in (a). Water is represented as transparent light blue surface.
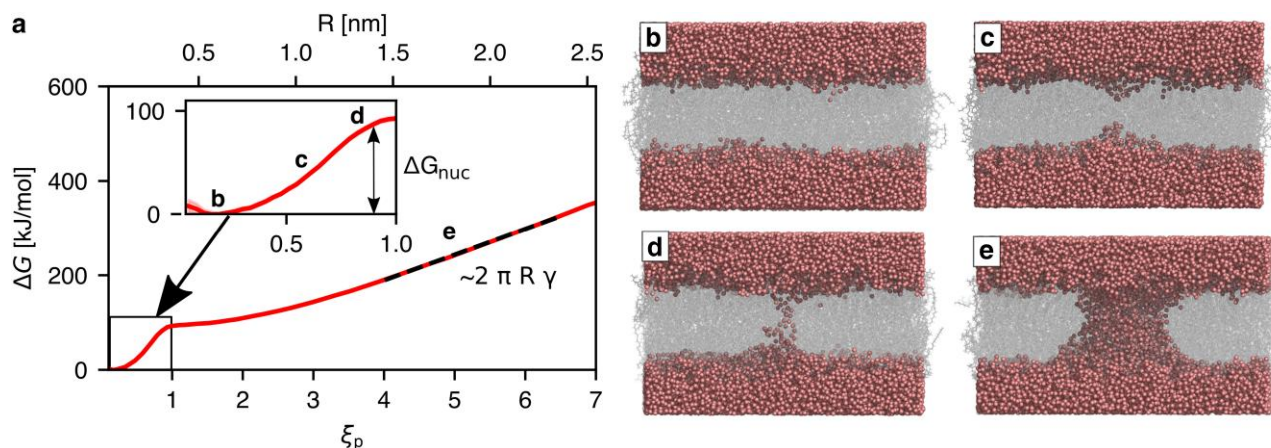

Fig. 2. Mechanism and energetics of pore formation. a) Example PMF of pore nucleation and expansion with the lipid composition of the Golgi apparatus, plotted either as function of the reaction coordinate ξ_p (lower abscissa) or of pore radius (upper abscissa). The inset shows a closeup view on the PMF during pore nucleation. The nucleation free energy ΔG_{nuc} was defined as the PMF value at $\xi_p = 0.92$, corresponding to the state with a thin water wire (vertical double arrow). The slope of the linear regime at $\xi_p > 4$ yields the line tension along the pore rim (black dashed line). Labels b–e indicate structures shown in (b–e). b) Simulation snapshot of umbrella windows with: a flat membrane ($\xi_p \approx 0.2$), c) a thinned membrane ($\xi_p \approx 0.7$), d) a thin water wire ($\xi_p \approx 0.9$), and e) a large pore with radius 1.8 nm ($\xi_p \approx 5$). Water oxygen atoms are shown as red spheres, lipids are represented as transparent gray sticks.

of the radius $R_0 \approx 0.4$ nm of a fully nucleated pore, i.e. $\xi_p = R/R_0$ (Fig. 2d–e). Figure 2a presents a typical PMF of pore formation, here shown for the membrane of the Golgi apparatus, plotted either as function of the reaction coordinate ξ_p (lower abscissa) or, for $\xi_p > 1$ where a transmembrane defect is present, as function of pore radius R (upper abscissa). Starting from the state of a flat membrane ($\xi_p = 0.2$, Fig. 2b), the PMF reveals an initial steep increase reflecting the energetic cost for membrane thinning ($\xi_p \approx 0.6$, Fig. 2c). A thin, transmembrane aqueous defect is formed at $\xi_p \approx 0.9$, thereby finalizing the pore nucleation phase (Fig. 2d). The plateau at $\xi_p \approx 1.5$ reflects some energetic stabilization by the tilting of lipids to form a toroidally shaped pore. After further expansion, at $\xi_p \gtrsim 4$ ($R \gtrsim 1.5$ nm), the PMF increases linearly reflecting mechanical work against an approximately constant

line tension γ along the pore rim (Fig. 2e). The shape of the PMF and the structural mechanisms involved in pore nucleation and expansion agree qualitatively with results obtained previously for simpler model membranes (20, 39, 40). Additional control simulations show that the PMFs are influenced by only minor hysteresis effects typically in the order of few kilojoules per mole (Fig. S1, Table T1). The linear regime of the PMF is compatible with classical nucleation theory (46, 47) that describes the free energy of larger pores by $\Delta G_{CNT} = 2\pi R\gamma - \pi R^2 \sigma$, where γ denotes the line tension along the pore rim of length $2\pi R$. The second term models the relief of surface tension σ owing to pore expansion. However, because our simulations were carried out at (i) constant pressure without external surface tension and (ii) at constant number of lipids, thereby keeping the membrane–
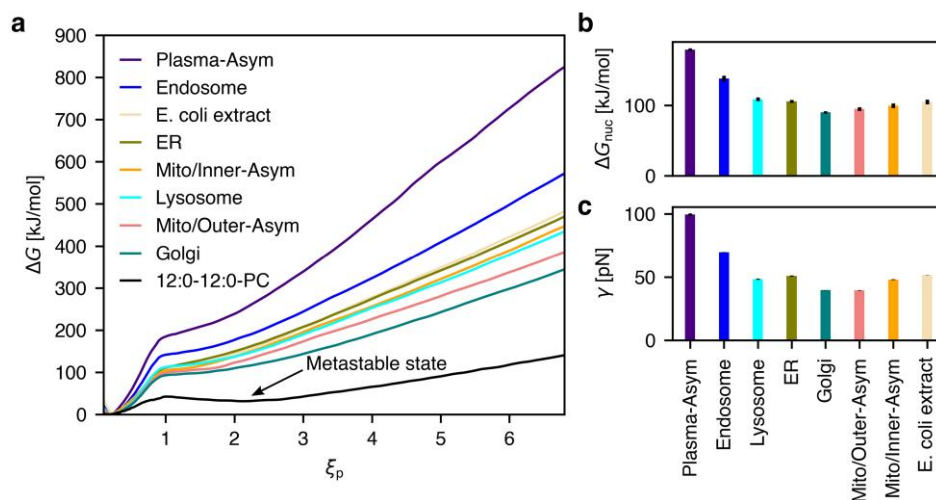
Fig. 3. Energetics of pore formation for eight complex membrane systems. a) PMFs for pore nucleation ($\xi_p \lesssim 0.92$) and pore expansion ($\xi_p \gtrsim 1$) in eight complex biological model membranes and in a membrane of pure di-12:0-PC (DLPC). The arrow highlights a local free energy minimum for the DLPC membrane, indicating a metastable open pore. b) Pore nucleation free energies ΔG_{nuc} and (c) line tension γ along the pore rim as taken from the PMFs. Error bars of ΔG_{nuc} and γ (hardly visible) obtained from bootstrapping (see Supplementary material) denote 1SE.

water interface area approximately constant, the second term can be neglected. Thus, the slope of the linear regime of the PMF at $\xi_p \gtrsim 4$ reflects the line tension γ and aligns with classical nucleation theory.

To characterize the energetics of pore nucleation and expansion, we extracted two quantities from the PMFs (see also Supplementary material). Firstly, we defined the pore nucleation energy ΔG_{nuc} as the free energy at $\xi_p = 0.92$, corresponding by the presence of a thin, stable transmembrane pore (Fig. 2a, inset, double arrow). Secondly, we obtained the line tension γ from the slope of a linear fit to the regime $4 \leq \xi_p \leq 6.5$ (Fig. 2a, dashed line). In the following, we use ΔG_{nuc} and γ to compare the free energy landscapes of pore formation of complex or simple model membranes.

Biological membranes greatly vary in their resistance against pore formation

Among the eight complex biological membranes simulated in this study, the PMFs of pore formation vary considerably (Fig. 3a, colored curves). The nucleation free energy ΔG_{nuc} varies between 90 kJ/mol for the Golgi membrane and 180 kJ/mol for the plasma membrane (Fig. 3b). The line tension γ varies between 40 pN for the Golgi membrane or for the mitochondrial outer membrane and 100 pN for the plasma membrane (Fig. 3c).

These large variations reflect the diverse biological functions of different membranes. Specifically, the plasma membrane is far more stable against pore formation when compared to membranes of intracellular organelles, thus highlighting its ability to form a barrier to the extracellular space. Such marked stability renders the plasma membrane robust against mechanical and osmotic stress, impedes the action of disruptive molecules such as bacterial pore-forming toxins, and forms a barrier against viral infection. In contrast, upwards the secretory pathway, membranes are increasingly unstable against pore formation, as evident from the low ΔG_{nuc} and γ values of the ER and Golgi membranes as well as, to a lower degree, of the lysosome membrane (Fig. 3b/c). The lower stability of these membranes aligns with their need for increased flexibility to enable ongoing remodeling, while not being exposed to the degree of mechanical stress that the plasma membrane needs to withstand. Similar arguments rationalize the

relatively low stability of the mitochondrial inner and outer membrane. A similarly low stability against pore formation is observed for the membrane formed by *E. coli* extract. However, in the physiological context, Gram-positive and Gram-negative bacteria are surrounded by peptidoglycan and lipopolysaccharide layers, respectively, which strongly contribute to robustness against mechanical stress (33, 48). Intermediate stability is observed for early endosomes, which derive from the plasma membrane (2). As shown below, the higher stability of the endosomal membranes is explained by their relatively high cholesterol content of ~30%, slightly above the cholesterol content of 25% of the inner plasma membrane leaflet. Notably, endosomal escape via membrane fusion may involve pore formation across hemifusion intermediate states. The considerable stability of endosomes may pose an additional challenge for the design of artificial endosomal escape systems, for instance in the context of RNA-based therapeutics delivered with lipid nanoparticles.

Biological membranes do not form metastable pores

Memory effects during early electroporation experiments suggested that lipid membranes may form metastable (long-living) pores (10) or, equivalently, that pores may represent a local minimum of the free energy landscape. Recently, MD simulations revealed that nanometer-sized pores are metastable only in membranes of inverted cone-shaped lipids (31). For instance, metastable pores are formed by lipids with short saturated tails such as lauroyl acid (di-12:0) or myristoyl acid (di-14:0) and bulky head groups such as PC or PG, whereas unstable pores are formed by lipids with unsaturated tails or smaller head groups form. Whether complex biological membranes form metastable pores has not been systematically addressed.

For reference, Fig. 3a (black curve) presents the PMF of pore formation for di-12:0-PC (DLPC). In agreement with previous studies (31, 39), the PMF for DLPC reveals a local free energy minimum at $\xi_p \approx 2.5$, implying a metastable pore of radius $R \approx 1$ nm. The presence of the metastable pore may imply pore lifetimes of microseconds or longer (19, 31). In sharp contrast, no such metastable pore was found in any of the complex membranes, as evident from the absence of corresponding local free energy minimum at $\xi_p > 1$

(Fig. 3a, colored curves). We hypothesize that the lipid composition of biological membranes has evolved to strictly avoid the formation of long-living pores, underlining that uncontrolled leakage of protons or other ions would be fatal for living cells. Thus, to form long-living pores even in biological membranes, external perturbations are required such as the application of large transmembrane potentials during electroporation experiments (20, 30) or the presence of membrane-active agents including channel-forming toxins(5), proteins involved in regulated cell death (7, 49), polymers (50), peptides (51, 52), or organic solvents such as DMSO (39, 53).

The outer leaflet of the plasma membrane is the main protection layer against pore formation

Next, we examined how lipid asymmetry influences pore formation in the plasma membrane and in the inner and outer mitochondrial membranes. To this end, we compared the PMFs obtained with asymmetric membrane models with PMFs obtained with symmetric membranes with the lipid composition of the respective outer or inner leaflet (Fig. S4). The PMFs revealed that the outer plasma membrane leaflet is far more stable compared to the inner leaflet, as shown by increased ΔG_{nuc} and γ values by 125 kJ/mol and 83 pN, respectively. These findings suggest that the outer plasma membrane leaflet serves as the primary protection layer against external stressors and against pore-forming agents. In contrast, the inner leaflet of the plasma membrane exhibits a lower stability with a nucleation barrier slightly below the value for the endosomal membrane, while still being more stable than the other biological membranes investigated in this study (Fig. S4).

The reduced stability of the inner plasma membrane leaflet aligns with its biological function. Exocytosis involves the formation of a hemifusion stalk between the inner leaflet of the plasma membrane and the outer leaflet of an intracellular vesicle, representing a major structural perturbation of the inner plasma membrane leaflet. Thus, the reduced stability of the inner leaflet against pore formation may provide a compromise between the ability to carry out structural remodeling with acceptable energetic costs while still contributing to the mechanical stability of the overall plasma membrane. These findings are consistent with our previous study that revealed that hemifusion stalk formation by the inner plasma membrane leaflet is far more energetically accessible than stalk formation by the outer leaflet (54).

The large difference in stability between the outer and inner plasma membrane leaflet is, in part, rationalized by the highly asymmetric cholesterol distribution in the plasma membrane model used here, (43) with cholesterol concentrations of 54% and 25% in the outer and inner leaflet, respectively. The influence of cholesterol on membrane stability is analyzed in detail below. In addition, sphingomyelin makes up 25% of the lipids of the outer leaflet (Fig. 1a). Since sphingomyelin increases lipid tail order and membrane stiffness as compared to PC lipids (55, 56), we hypothesized that sphingomyelin enrichment contributes to the great stability of the plasma membrane outer leaflet. Indeed, by comparing the PMF for a pure POPC membrane with the PMF for a 1:1 mixture of POPC with 18:0–24:0-sphingomyelin (DSM), we found that the addition of DSM increases ΔG_{nuc} by 40 kJ/mol (Fig. S5). Thus, cholesterol and sphingomyelin contribute to the marked stability of the outer plasma membrane leaflet.

Whereas the two plasma membrane leaflets reveal greatly different stabilities against pore formation, this is not the case for the mitochondrial membranes. Namely, despite the marked asymmetry of the mitochondrial inner and outer membranes (Fig. 1a), symmetric membranes with the composition of the inner or outer leaflet reveal nearly identical ΔG_{nuc} and only minor variations of γ

values (Fig. S4b–e). These findings likely reflect that mitochondrial membranes, relative to the plasma membrane, are faced with far lower mechanical stress.

Lipid-specific enrichment or depletion modulate the rim energy

Based on the observation that the addition of a lipid species such as sphingomyelin may strongly alter the free energy of pore formation, we investigated the spatial distribution of lipid species during pore formation. From 400 ns simulations of open pores, we computed the mass densities of several lipid species as function of lateral distance r from the pore center and normal distance z from the membrane center. Densities were computed for membranes with the composition of the Golgi apparatus (Fig. 4b–i), outer plasma membrane leaflet, endosome, and *E. coli* extract (Fig. S6). The densities reveal enrichment or depletion at the pore rim by several lipid species.

The toroidal pore rim is characterized by Gaussian curvature with positive curvature along the membrane normal and negative curvature in the membrane plane. Whether the positive or the negative component of the rim curvature controls lipid enrichment and depletion is, a priori, not obvious. Among the Golgi membrane lipids, we found that lyso-PC was enriched at the pore rim (Fig. 4b/f), where lyso-PC preferentially adopted a tilted conformation, thereby shielding the hydrophobic membrane core from the transmembrane water defect (Fig. 4a, black arrow). Because lyso-PC is characterized by a large head-to-tail volume ratio, lyso-PC stabilizes positive membrane curvature (57). Lyso-PC enrichment at the pore was likewise observed in simulations of binary POPC/lyso-PC mixtures (Fig. S7). These findings suggest that the positive curvature along the membrane normal dominates the pore energy and, thereby, controls lipid enrichment or depletion at the pore rim, even for small pores with radius of ~1 nm (Figs. 4a, S7) and considerable Gaussian curvature. Thus, lipids with positive intrinsic curvature such as lyso-PC may stabilize pores. For instance, lyso-PC likely contributes to the low line tension of pores in the Golgi membrane (Fig. 3c).

In contrast to lyso-PC, cholesterol and sphingomyelin were depleted from pores in Golgi, *E. coli* extract, plasma, and endosomal membranes (Figs. 4a, c/d, g/h and S6), and oleic acid was depleted from pores across POPC/olecic acid membranes (Fig. S7). Thus, the geometries of cholesterol, sphingomyelin, and oleic acid are incompatible with the rim structure, which aligns with the large free energies of pore formation in the plasma membrane model, which contains large amounts of sphingomyelin and cholesterol, and with the increased free energies in the POPC/olecic acid membranes (Fig. S7). Thus, enrichment or depletion of specific lipids at the pore rim correlate with stabilizing or destabilizing lipid effects, respectively.

Notably, lateral sorting may lead to different specific lipid concentrations at the pore rim relative to the bulk membrane. Consequently, elastic membrane properties such as bending moduli derived from bulk membranes are not necessarily applicable to the pore rim in complex multicomponent membranes.

Among eukaryotic membranes, sterol concentration is a major regulator of membrane stability

Which structural lipid properties control ΔG_{nuc} and γ, and which lipid properties are employed by biological cells to tune membrane stability? To answer these questions, we investigated systematically how ΔG_{nuc} and γ are modulated by three structural
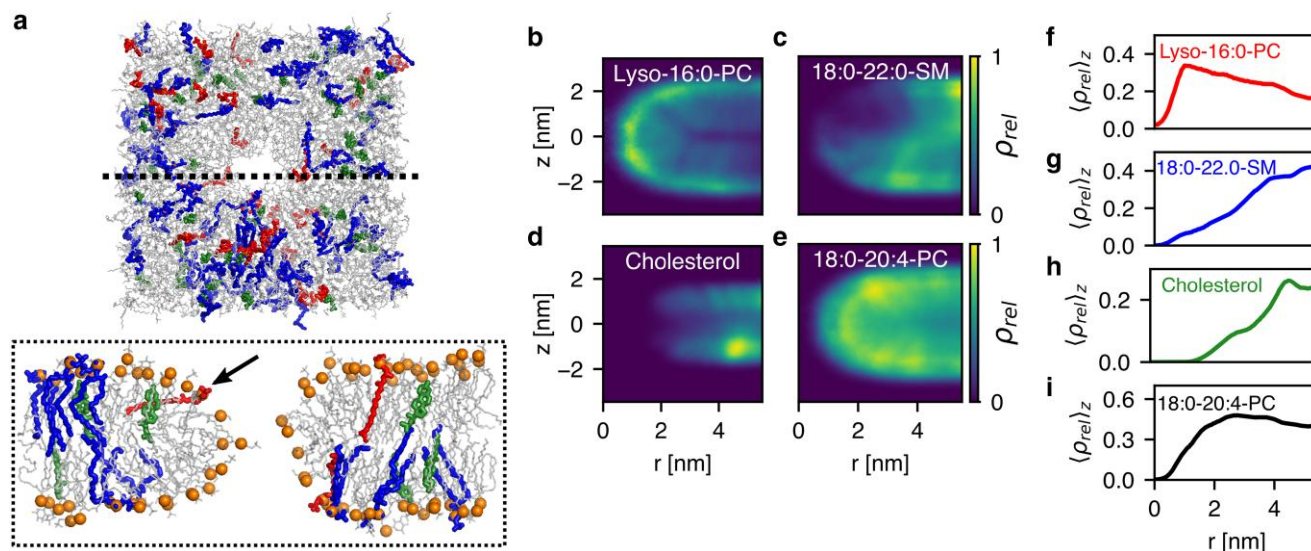
Fig. 4. On lipid-specific enrichment or depletion at the pore rim. a) Simulation snapshot with lipid composition of the Golgi apparatus with a pore with radius $R = 1.3$ nm in top view (upper panel) and side view (lower panel). Lipids are shown as sticks, with phosphorous atoms highlighted as orange spheres. Lyso-16:0-PC, cholesterol, and sphingomyelin are shown as red, green, and blue thick sticks, respectively, and other lipids as thin gray sticks. The arrow highlights a tilted lyso-16:0-PC lipid at the pore rim. b–e) Lipid density along the pore rim as function of radial distance r from the pore center and normal distance z from the membrane center, relative to the density in the bulk membrane, for b) lyso-16:0-PC, c) 18:0–22:0-sphingomyelin, d) cholesterol, and e) 18:0–20:4-PC. f–i) 1D lipid density profiles after averaging the densities in (b–e) along z.

properties that have been implicated with membrane stability: sterol content (24, 25), lipid tail length (22, 23), and degree of unsaturation (34). We computed PMFs for twelve model membranes (Fig. S9a–c) and compared the derived ΔG_{nuc} and γ values (Fig. 5g–l) with the values obtained for complex biological membranes (Fig. 5a–f).

The addition of cholesterol to a membrane of POPC leads a marked concentration-dependent increase of ΔG_{nuc} and γ by up to 100 kJ/mol and 35 pN, respectively (Fig. 5g/j), which aligns with the trends in complex membranes (Fig. 5a/d). Likewise, by increasing the tail length among five simulations with lipids from di-14:1-PC up to di-22:1-PC, ΔG_{nuc} and γ increase considerably (Fig. 5h/k), likely owing to increasing membrane thickness (22, 23, 58). Thus, both sterol content and tail length modulate membrane stability against pore formation. However, among the biological membranes studied here, whereas cholesterol content varied between 0 and 54% (Fig. 5a/d), the average lipid tail length varied only between 16.7 and 18.8 carbons (Fig. 5e/k, red arrows). These findings suggest that, among the eukaryotic membranes studied here, not the tail length but instead the sterol content serves as the key regulator for membrane stability. While many prokaryotes do not contain sterols, a similar membrane-stiffening effect has been attributed to hopanoids, (59) suggesting that hopanoids may play a similar role in membrane stability of prokaryotes.

A recent simulation study based on the coarse-grained MARTINI model reported that poration across complex biological membranes occurs predominantly at sites with a local enrichment of polyunsaturated lipids (34). To test the effects of unsaturation on pore formation with atomistic models, we obtained ΔG_{nuc} and γ for lipids with increasing degree of unsaturation: 18:0–18:1-PC, di-18:1-PC, di-18:2-PC, or 18:2–18:3-PC. We found that the degree of unsaturation has only a small effects on membrane stability against pore formation, thus challenging the interpretation of the coarse-gained simulations (34). While ΔG_{nuc} was virtually invariant with respect to unsaturation (Fig. 5i), γ revealed an initial rise upon the addition of a second double bond, followed

by a minor decrease upon the addition of two or three double bonds per lipid (Fig. 5l). These effects may be rationalized by two opposing effects: on the one hand, a higher degree of unsaturation leads to membrane thinning (Fig. S8b), in line with experimental observations (60), which would lead to decreasing ΔG_{nuc} and γ. On the other hand, owing to the kinks in the acyl chains, polyunsaturated lipids induce negative membrane curvature, which is incompatible with positive curvature along the membrane normal, which dominates the pore energy as well as lipid enrichment and depletion, as discussed above. Thus, effects by polyunsaturated lipids on membrane thickness may cancel with curvature effects, rationalizing the overall small influence on the free energies of pore formation.

Pore line tension correlates with Helfrich bending energy while nucleation free energy correlates with lipid tilt modulus

Complementary to MD simulations, elasticity theory has been applied to model the free energy of toroidal open pores with contributions from membrane bending, membrane stretching, or lipid tilt (18, 21, 41, 42, 61). The HKH free energy functional (41, 42) relates the physical properties of lipid monolayers and flat bilayers to the energy of their deformations:

$$F = \int dA \left[\frac{1}{2}\kappa(\tilde{H} - J_s)^2 + \frac{1}{2}\kappa_\theta \mathbf{t}^2 + \bar{\kappa}\tilde{K}_G \right]. \tag{1}$$

According to the functional, F is determined by the bending modulus κ that is associated with the difference between the sum $\tilde{H}$ of the two principal curvatures and the spontaneous curvature J_s. The tilde on $\tilde{H}$ highlights that the calculation is performed over the director field, rather than over the membrane normal vectors. The tilt modulus κ_θ is associated with the local lipid tilt vector $\mathbf{t}$ defined by the deviation of lipid orientation vector $\mathbf{d}$ from the membrane normal $\mathbf{n}$ (Fig. 6c). In the absence of tilt, F equals the common Helfrich functional (42). The Gaussian curvature $\tilde{K}_G$ and its associated modulus $\bar{\kappa}$ are typically ignored in studies of
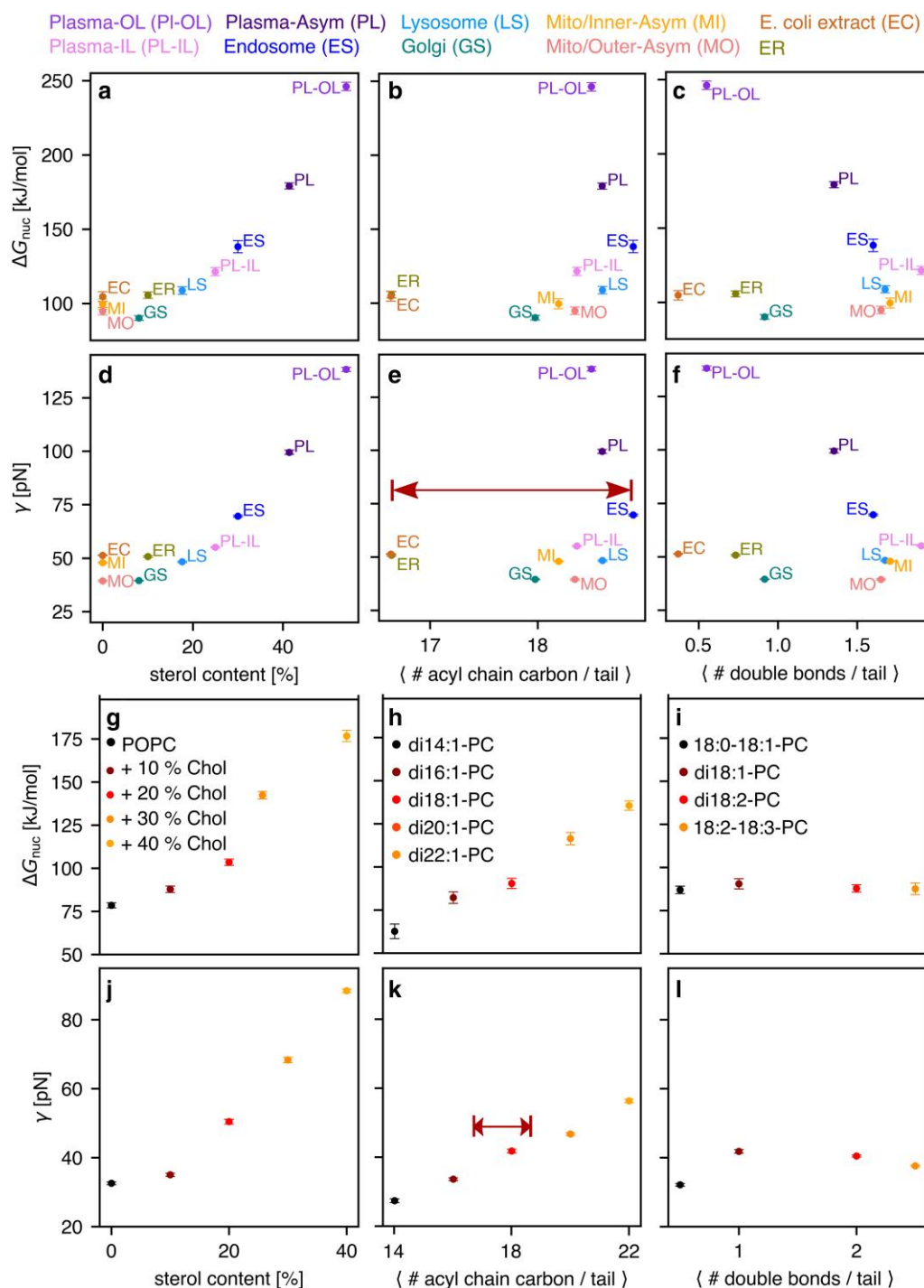
Fig. 5. On the effects of sterol concentration (left column), lipid tail length (middle column), and tail unsaturation (right column) on pore nucleation free energy ΔG_{nuc} and line tension γ. a–f) Correlation plots (see axis labels) for biological membranes, with abbreviations defined in the upper row. g–l) Correlation analysis among the same pairs of quantities as shown in (a–f), however analyzed for model membranes of g/j) POPC with cholesterol content between 0 and 40%, h/k) membranes with increasing tail length (see legend), or i/l) membranes with increasing unsaturation, plotted as number of double bonds per acyl chain (see legend). Arrows in (e) and (k) highlight the range of average tail lengths realized by biological membranes.

membrane deformations as, according to the Gauss–Bonnet theorem, the integral over $\tilde{K}_G$ for a closed surface is a topological invariant. However, the formation of a pore changes the topology of the membrane and involves the formation of an additional boundary, hence this modulus is potentially relevant for pore formation. The HKH theory of membrane elasticity (Eq. 1) can only be expected to provide semiquantitative insight into pore formation for several reasons. First, it is not evident whether the pore rim

is to be modeled as curved monolayer or as a hole whose boundary is formed by a large number of tilted lipids. Second, Helfrich theory may be taken as a series expansion of the free energy up to second order around a flat reference geometry; thus, whether the theory is applicable to a highly curved pore rim is unclear. Third, for small pores, details of hydrogen bond networks, the finite size of water molecules, and electrostatic interactions may be important (20). Nonetheless, the theory has been applied to
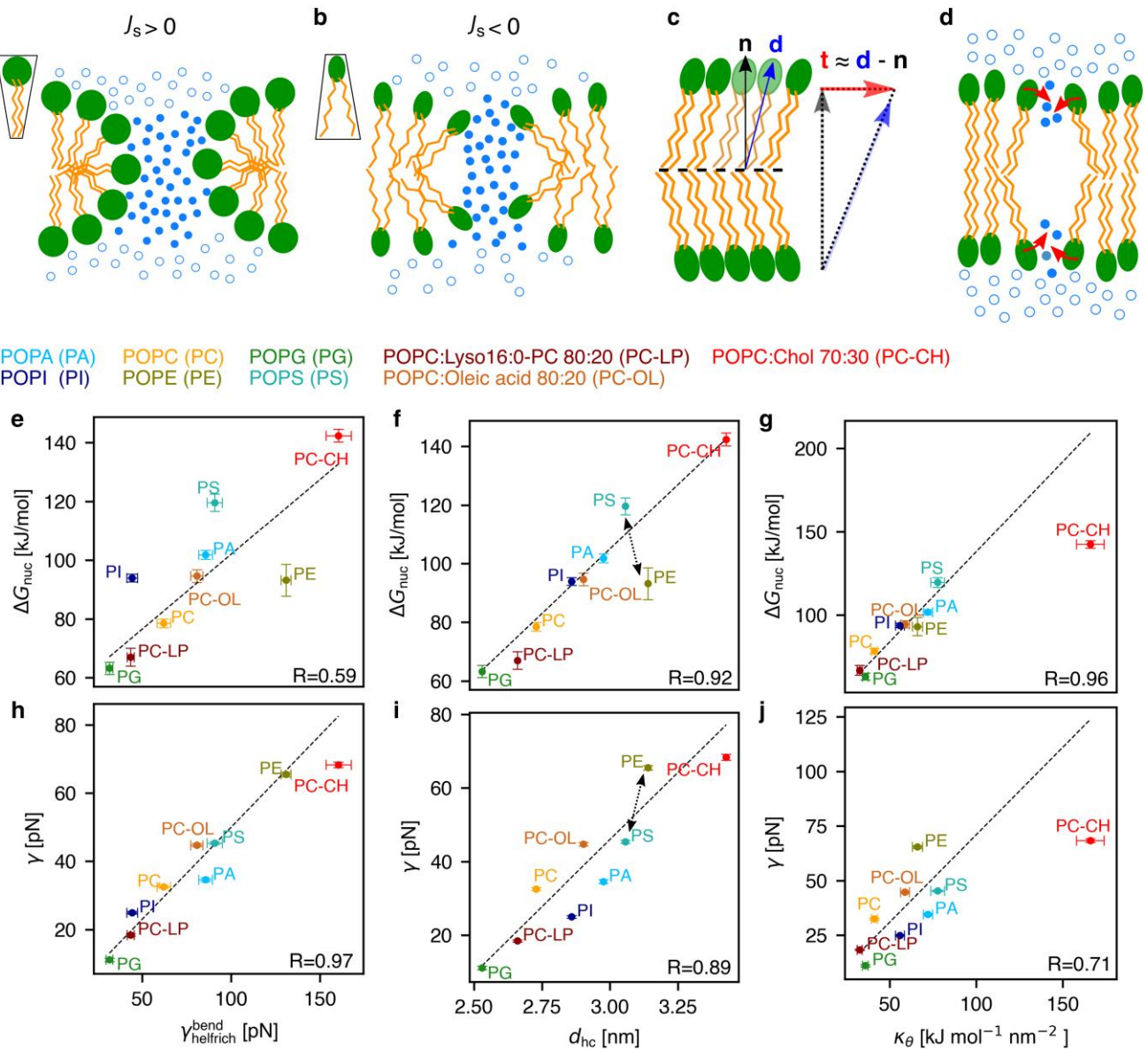
Fig. 6. Influence of elastic and geometric properties of the membrane on nucleation free energy ΔG_{nuc} and line tension γ. a) Inverted cone-shaped lipids with positive spontaneous curvature J_s enable favorable packing along the pore rim, whereas b) cone-shaped lipids with negative J_s reveal unfavorable packing along the rim. Contribution of bending is characterized by $\gamma_{\text{Helf}}^{\text{bend}}$. c) Definition of lipid tilt vector $\mathbf{t} = \mathbf{d}/(\mathbf{n} \cdot \mathbf{d}) - \mathbf{n} \approx \mathbf{d} - \mathbf{n}$, with $\mathbf{n}$ denoting the membrane normal vector and $\mathbf{d}$ the director. d) Illustration of lipid tilting during pore nucleation, with lipid tilting being capable of stabilizing the initial aqueous defect. e/h, f/i, g/j) Correlations of ΔG_{nuc} or γ with $\gamma_{\text{Helf}}^{\text{bend}}$, hydrophobic core thickness d_{hc} and tilt modulus κ_θ (see axis labels) for six palmitoyl-oleoyl (PO, 16:0–18:1) membranes with varying head groups of PA, PI, PG, PC, PE, or PS, as well as 80:20 mixtures of POPC with 16:0-lyso-PC (PC-LP) or with oleic acid (PC-OL) and a 70:30 mixture of POPC and cholesterol (PC-CH). Results of a linear regression excluding the POPC/cholesterol data points are shown as dashed lines and correlation coefficients R (see Table S11). Dashed arrows (f/i) highlight reversed effect of PS and PE head groups on ΔG_{nuc} and γ.

model pore formation via a variational minimization of the HKH functional with variable pore boundary geometry using a boundary condition in the director orientation (18).

In this study, we do not aim to explain pore free energies quantitatively by HKH theory. Instead, we correlate pore free energies from PMF calculations to lipid properties in the context of the HKH theory (such as spontaneous curvature, bending, or tilt moduli), with the aim to reveal the physicochemical determinants of membrane stability. To this end, by means of a back-of-the-envelope estimation, membrane bending contributes to the free energy of large pores via the term $\kappa(\tilde{H} - J_s)^2/2$ (see Eq. 1), where $\tilde{H}$ is the large positive curvature along the pore, while J_s is the spontaneous curvature. The effect of J_s on pore formation has frequently been interpreted

geometrically: (62) inverted-cone shaped or cone-shaped lipids impose positive or negative J_s, thereby enabling either favorable or unfavorable packing along the pore rim, respectively (Fig. 6a/b). For instance, unsaturated fatty acids such as oleic acid with a bulky tail and a small polar head group impose negative J_s, whereas saturated mono acyl lipids such as lyso-16:0-PC impose positive J_s (63). Thus, oleic acid and lyso-16:0-PC are expected to impede or to facilitate pore formation, respectively, which we confirmed by a series of PMF calculations with membranes with increasing oleic acid or lyso-PC content (Fig. S7). Lipids with $J_s \approx 0$ such as POPC are associated with a cylindrical shape, thus expected to show intermediate behavior. Integrating the bending energy functional (first term in Eq. 1) over the rim of a large pore (21) yields the line tension

Table 1. Spontaneous curvature J_s, monolayer bending modulus κ, and bilayer tilt modulus κ_θ computed from planar membranes as well as estimated line tension from Helfrich theory $\gamma_\mathrm{Helf}^\mathrm{bend}$.

Component	J_s [nm^{-1}]	κ [kJ mol^{-1}]	κ_θ [kJ mol^{-1} nm^{-2}]	$\gamma_\mathrm{Helf}^\mathrm{bend}$ [pN]
POPC (66)	-0.001 ± 0.028	33.7 ± 1.4	42.53 ± 1.7	62 ± 4
POPE (67, 68)	-0.178 ± 0.005	48.0 ± 0.9	65.6 ± 2.9	130 ± 3
POPA	0.027 ± 0.006	53.1 ± 2.3	72.1 ± 2.7	86 ± 4
POPI	0.172 ± 0.016	42.8 ± 2.1	55.8 ± 2.6	44 ± 3
POPG	0.227 ± 0.017	30.2 ± 1.3	35.8 ± 1.6	32 ± 2
POPS	-0.019 ± 0.007	50.3 ± 2.3	78 ± 4	91 ± 5
POPC:lyso16:0-PC 80:20	0.085 ± 0.008	28.2 ± 1.2	32.6 ± 1.4	43 ± 2
POPC:oleic acid 80:20	-0.063 ± 0.009	37.7 ± 1.5	58.8 ± 2.5	81 ± 4
POPC:Chol 70:30	-0.0007 ± 0.003	105 ± 5	166 ± 8	160 ± 8

$\gamma_\mathrm{Helf}^\mathrm{bend} = \kappa d_\mathrm{hc}\pi/4 \cdot (2/d_\mathrm{hc} - J_\mathrm{s})^2$, where d_hc denotes the thickness of the membrane hydrophobic core. Here, it was assumed that one principal curvature is given by $c_1 = 1/(d_\mathrm{hc}/2)$, whereas the second principal curvature is approximately zero for a large pore. Following previous work (21), we hypothesized that the line tension γ obtained from simulations may be correlated with the line tension $\gamma_\mathrm{Helf}^\mathrm{bend}$ suggested by elasticity theory.

In contrast to wide open pores, the defects during the pore nucleation phase do not adopt a toroidal shape but are instead characterized by thin aqueous protrusions into the hydrophobic membrane core (Fig. 2c) (19, 27–30, 39, 64, 65). Visual inspection of the simulations revealed that such aqueous protrusions are stabilized by partial tilting of lipids, thereby reducing the unfavorable contact of the aqueous protrusion with the membrane core (Fig. 6c/d) (17, 39). Thus, we hypothesized that the free energy of pore nucleation is, in addition to membrane thickness (22, 31), controlled by the energy of lipid tilting as given by the term $\frac{1}{2}\kappa_\theta\mathbf{t}^2$ in the HKH functional (Eq. 1).

To systematically investigate the roles of bending and tilting during pore formation, we resorted to simple model membranes of various lipid compositions: single-component model membranes with the same palmitoyl-oleoyl (PO) tails combined with different head groups, namely POPC, POPE, POPS, POPA, and POPG, as well as binary mixtures of POPC with either cholesterol or with the curvature-inducing single-tailed lyso-16:0 PC or oleic acid. From simulations of planar membranes, we computed J_s, κ, and κ_θ, where values for POPC and POPE were taken from previous studies (66–68). Table 1 demonstrates large variations of J_s in the range between -0.18 nm^{-1} for POPE, characterizing a cone-shaped lipid (69), up to 0.23 nm^{-1} for POPG, characterizing an highly inverted-cone-shaped lipid. As expected, the addition of lyso-16:0-PC or oleic acid to POPC imposes positive or negative J_s, respectively, whereas the effect of cholesterol is hardly detectable within our statistical errors (63, 70). Likewise, both the bending modulus κ and the tilt modulus κ_θ vary considerably among the model membranes, characterizing harder or softer bending or tilt deformations, respectively. Notably, the addition of 30% cholesterol leads to a strong hardening of both bending and tilt deformations as shown by the by far largest κ and κ_θ values. As shown in the following, the variations in J_s, κ, and κ_θ have large effects on the free energies of pore formation.

Figure 6e–j correlates ΔG_nuc or γ obtained from PMFs of pore formation with elasticity properties obtained from simulations of planar membranes. Here, for the calculation of correlation coefficients R, we excluded the POPC/cholesterol membrane because cholesterol is nearly completely depleted from the pore rim (Fig. 4d and h). In line with our hypothesis stated above, the line tension along the pore rim γ strongly correlates with the line tension from HKH theory $\gamma_\mathrm{Helf}^\mathrm{bend}$ (Fig. 6h, correlation coefficient $R = 0.97$); however, the simple integration of the HKH energy

functional as carried out here overestimates the line tension by a factor of approximately two, thus emphasizing the need for a consistent minimization including tilt degrees of freedom. The membrane thickness and tilt modulus reveal weaker correlation with γ (Fig. 6i/j). This analysis suggests that bending deformation energy is the key contribution to the pore line tension in agreement with previous work (18).

In contrast, ΔG_nuc reveals poor correlation with $\gamma_\mathrm{Helf}^\mathrm{bend}$ (Fig. 6e) but instead strongly correlates with tilt modulus κ_θ (Fig. 6g, $R = 0.96$). This suggests that soft lipid tilting as found in membranes POPG or POPC:lyso-PC facilitates pore nucleation because head group tilting may stabilize water protrusions into the membrane core, as illustrated in Fig. 6d. Notably, in agreement with previous simulation studies (22, 31), ΔG_nuc furthermore strongly correlates with membrane thickness d_hc. However, the correlation with d_hc is weaker compared to the correlation with κ_θ, mostly because POPE reveals smaller ΔG_nuc than POPS albeit forming a thicker membrane (Fig. 6f, black arrow). Thus, in addition to membrane thickness, lipid tilting energy emerges as a key determinant for pore nucleation. The importance of thickness and tilting may be expected because they are both proxies for packing of the lipid tails. However, because only the tilt modulus quantifies a cost for modifying the lipid tail packing, the tilt modulus is the better descriptor for the energetic cost of pore formation during which the lipid chain configuration changes dramatically.

Discussion

We presented PMF calculations of pore formation across complex biological membranes and across simple single- or two-component model membranes, providing two principal energetic parameters: the nucleation free energy ΔG_nuc and the line tension γ along the rim of large pores. The results for γ obtained here with the CHARMM36 lipid force field are in reasonable agreement with experiments that reported values between 6.7 and 39.5 pN for various lipid compositions (Table S12) (26, 71–75). However, quantitative comparison is challenging considering that experimental values vary considerably; for instance, reported γ values for DOPC vary by up to a factor of four depending on the lipid supplier and reference, which has been attributed to the presence of small amounts of impurities (72, 73). Nevertheless, trends of γ with varying lipid composition observed here agree with previous reports: specifically, γ decreased upon replacing PE with PC head groups or by replacing two-tailed PC lipids with lyso-PC (74). Likewise, the exceptionally low γ and ΔG_nuc obtained here for POPG aligns with Lira et al. (26), who reported a marked destabilization of giant unilamellar vesicles (GUV) upon the addition of 50% POPG to a membrane of POPC. Notably, Lira et al. suggested that the low stability of POPG-containing GUVs may indicate general feature of membranes with anionic lipids. In our simulations,

in contrast, membrane destabilization was specific for POPG owing to (i) its exceptionally low tilt modulus κ_θ, leading to low ΔG_{nuc} and (ii) its low bending modulus κ together with a large spontaneous curvature J_s, leading to low line tension γ (Fig. 6, Table 1, and Table S13). Membranes formed by other anionic lipids POPI, POPA, and POPS exhibited larger ΔG_{nuc} and γ values, which aligns for the case of POPS with previous experimental and computational studies (76, 77). However, considering that force fields for anionic lipids have not been refined against experiments as extensively as force fields for zwitterionic lipids, it will be important to revisit the role of anionic lipids during pore formation in future studies.

The nucleation free energies ΔG_{nuc} reported above determine the probabilities of pore formation in the small simulation system used during pore nucleation via $P_{\text{pore}}^{\text{sim}} \approx \exp\left(-\Delta G_{\text{nuc}}/k_B T\right)$, where k_B and T denote the Boltzmann constant and temperature, respectively. Because the probability of pore formation is proportional to the membrane area, the simulation conditions translate to the free energy of pore formation under experimental conditions of

$$\Delta G_{\text{nuc}}^{\text{exp}} = \Delta G_{\text{nuc}} - k_B T \ln\left(A_{\text{exp}}/A_{\text{sim}}\right),$$

where A_{exp} and A_{sim} denote the membrane areas in experiment and in our small simulation system, respectively. For instance, for a large GUV of POPG with radius $100\,\mu\text{m}$, $\Delta G_{\text{nuc}}^{\text{exp}}$ would equal only $9\,\text{kJ/mol}$, implying frequent water leakage. For the Golgi apparatus with a membrane area of approximately $1000\,\mu\text{m}^2$, $\Delta G_{\text{nuc}}^{\text{exp}}$ takes a considerable value of $48\,\text{kJ/mol}$, implying a probability of pore formation of 10^{-9} in the absence of any membrane stress (78). Thus, considering that the Golgi membrane revealed the smallest ΔG_{nuc} value among the biological membranes studied here, these results demonstrate that even biological membranes of inner cellular compartments are remarkably stable, possibly to withstand structural perturbations caused by membrane-associated proteins as well as mechanical stress during membrane remodeling. The stability of the plasma membrane is increased by another $\sim 80\,\text{kJ/mol}$ relative to the membranes of the inner compartments mostly owing to the high cholesterol and sphingomyelin contents of its outer leaflet, implying another reduction of pore probability by a factor of 10^{13} in the absence of stress. Such marked stability has likely evolved to withstand major mechanical stress faced by biological cells and, possibly, to reduce the risk of bacterial or viral infection.

We identified cholesterol content as a potent regulator for the stability of the biological membranes studied here. Cholesterol greatly increases γ by increasing the bending modulus κ (Table 1, Fig. 6) and by moderately increasing the membrane thickness, implying a large bending energy along the pore rim in the context of Helfrich theory. In addition, cholesterol greatly increases ΔG_{nuc} by increasing the tilt modulus κ_θ. Cholesterol has also been associated with negative membrane curvature (70, 79, 80), which could be taken as an indication that cholesterol intrinsic curvature contributes to the increased pore free energies since it would be incompatible with the large positive curvature along the membrane normal of the pore rim. Our data and previous results do not support this interpretation. First, compared to (i) the large effect of cholesterol on κ and κ_θ and (ii) large variations of J_s among phospholipids, the effect of cholesterol in a POPC membrane on spontaneous curvature J_s is small (Table 1). Second, cholesterol is not only depleted from positively curved pore rims as reported here but also from negatively curved fusion stalks as shown previously (54). The depletion of cholesterol from highly curved membrane regions is therefore not explained by intrinsic cholesterol curvature but, more likely, by unfavorable

interactions of cholesterol with the disordered lipid tail structures along pores or stalks. Together, our results suggest that the membrane-stabilizing cholesterol effect against pore formation is predominantly a consequence of the increase in membrane stiffness against bending and tilting deformations, whereas effects of cholesterol on spontaneous curvature play only a minor role during pore formation. Notably, the γ and ΔG_{nuc} values for the POPC:cholesterol 70:30 membrane are lower than expected from the correlation analysis among other model membranes; we rationalize this finding by lateral depletion of cholesterol from the pore rim (Figs. 4d and h and 6e–j).

Conclusion

Any form of life relies on tightly controlled compartmentalization by lipid membranes. To quantify the robustness of lipid membranes against mechanical stress, we computed the free energy landscape of pore formation across eight different complex biological membranes, revealing that, both, the nucleation free energy ΔG_{nuc} and the line tension along the pore rim γ vary greatly among biological membranes. The plasma membrane, and in particular its outer leaflet, is far more stable against pore formation as compared to membranes of intracellular compartments, as shown by ΔG_{nuc} and γ values increased by $\sim 125\,\text{kJ/mol}$ and $\sim 83\,\text{pN}$, respectively. However, even membranes of intracellular compartments are remarkably stable against pore formation, quantified by the probability of pore formation per cell in the order of 10^{-9} in the absence of stress, and given that none of the biological membranes studied here form metastable pores. We found that, while membrane stability may in principle be enhanced either by increased sterol content or by incorporating longer lipid tails, mainly the sterol content is utilized to regulate the wide range of membrane stabilities among the eukaryotic membranes studied here. Sterol enhances membrane stability via simultaneously increasing membrane thickness, the tilt modulus, and the bending modulus, but not primarily via imposing negative curvature. Compared to sterol content and tail length, lipid polyunsaturation has only a small effect on membrane stability. In complex membranes, the pore free energies may be decreased considerably by enriching or depleting lipids with positive or negative intrinsic curvature at the pore rim, respectively, suggesting that mechanical properties obtained for planar membranes may not be applicable to the pore rim region.

To scrutinize the lipid properties that control membrane stability, we computed, for a large set of simpler model membranes, the PMFs of pore formation as well as parameters of membrane elasticity theory, namely the spontaneous curvature, bending modulus, and tilt modulus. We found that γ is highly correlated to the bending energy over the pore rim, whereas the biologically important nucleation free energy is primarily determined by the tilt modulus because lipid tilting may reduce the cost of water penetration into the hydrophobic membrane core. Together, our simulations provide an energetic and mechanistic view on transmembrane pore formation, and they reveal how biological cells utilize complex lipid compositions to tune the mechanical stability of membranes, as required for robust compartmentalization.

Method summary

MD simulations were carried out using GROMACS (81). PMF calculations of pore formation were carried out using umbrella sampling (US) along a joint reaction coordinate for pore nucleation and expansion (39, 40, 82) implemented in a modified GROMACS

version freely available at https://gitlab.com/cbjh/gromacs-chain-coordinate. Lipids were described with the CHARMM36 force field (83–87). Continuum properties, i.e. spontaneous curvature, bending modulus, and tilt modulus were computed from equilibrium simulations of planar membranes as described previously (66, 67, 88). Lipid director definitions as part of the LIPIDATOR-TOOLKIT and a modified GROMACS version to calculate the local stress tensor are freely available at https://github.com/allolio. Additional computational details are described in the Supplementary material, which contains the additional Refs. (89–107).

Acknowledgments

Supplementary Material

Supplementary material is available at *PNAS Nexus* online.

Funding

Author Contributions

L.J.S.: Investigation; Methodology; Writing-original draft; Writing-review and editing; C.A.: Resources; Software; draft; Writing-review and editing; J.S.H.: Conceptualization; Resources; Software; Supervision; Funding acquisition; Methodology; Writing.

Data Availability

A modified GROMACS code that implements the reaction coordinate for pore formation is available at https://gitlab.com/cbjh/gromacs-chain-coordinate. Code for computing mechanical properties of membranes from MD simulations is available at https://github.com/allolio. Simulation systems together with instructions on how to run pore-opening simulations have been deposited in Zenodo at https://doi.org/10.5281/zenodo.13998169.

An early version of this study has been published on bioRxiv (108).

References

1 Shevchenko A, Simons K. 2010. Lipidomics: coming to grips with lipid diversity. *Nat Rev Mol Cell Biol*. 11(8):593–598.

2 Van Meer G, Voelker DR, Feigenson GW. 2008. Membrane lipids: where they are and how they behave. *Nat Rev Mol Cell Biol*. 9(2): 112–124.

3 Devaux PF. 1991. Static and dynamic lipid asymmetry in cell membranes. *Biochemistry*. 30(5):1163–1173.

4 Op Den Kap JAF. 1979. Lipid asymmetry in membranes. *Ann Rev Biochem*. 48(1):47–71.

5 Peraro MD, Van Der Goot FG. 2016. Pore-forming toxins: ancient, but never really out of fashion. *Nat Rev Microbiol*. 14(2): 77–92.

6 Brogden KA. 2005. Antimicrobial peptides: pore formers or metabolic inhibitors in bacteria? *Nat Rev Microbiol*. 3(3):238–250.

7 Flores-Romero H, Ros U, Garcia-Saez AJ. 2020. Pore formation in regulated cell death. *EMBO J*. 39(23):e105753.

8 Chabanon M, Ho JC, Liedberg B, Parikh AN, Rangamani P. 2017. Pulsatile lipid vesicles under osmotic stress. *Biophys J*. 112(8): 1682–1691.

9 Dias C, Nylandsted J. 2021. Plasma membrane integrity in health and disease: significance and therapeutic potential. *Cell Discov*. 7(1):4.

10 Abidor IG, et al. 1979. Electric breakdown of bilayer lipid membranes I. The main experimental facts and their qualitative discussion. *Bioelectrochem Bioenerg*. 6(1):37–52.

11 Kotnik T, et al. 2015. Electroporation-based applications in biotechnology. *Trends Biotechnol*. 33(8):480–488.

12 Eremchev M, et al. 2023. Passive transport of Ca2+ ions through lipid bilayers imaged by widefield second harmonic microscopy. *Biophys J*. 122(4):624–631.

13 Roesel D, Eremchev M, Poojari CS, Hub JS, Roke S. 2022. Ion-induced transient potential fluctuations facilitate pore formation and cation transport through lipid membranes. *J Am Chem Soc*. 144(51):23352–23357.

14 Sengel JT, Wallace MI. 2016. Imaging the dynamics of individual electropores. *PNAS*. 113(19):5281–5286.

15 Kotnik T, Rems L, Tarek M, Miklavčič D. 2019. Membrane electroporation and electropermeabilization: mechanisms and models. *Annu Rev Biophys*. 48:63–91.

16 Bennett WD, Tieleman DP. 2014. The importance of membrane defects lessons from simulations. *Acc Chem Res*. 47(8): 2244–2251.

17 Bubnis G, Grubmüller H. 2020. Sequential water and headgroup merger: membrane poration paths and energetics from md simulations. *Biophys J*. 119(12):2418–2430.

18 Akimov SA, et al. 2017. Pore formation in lipid membrane II: energy landscape under external stress. *Sci Rep*. 7(1):12509.

19 Awasthi N, Hub JS. 2016. Simulations of pore formation in lipid membranes: reaction coordinates, convergence, hysteresis, and finite-size effects. *J Chem Theory Comput*. 12(7):3261–3269.

20 Kasparyan G, Hub JS. 2024. Molecular simulations reveal the free energy landscape and transition state of membrane electroporation. *Phys Rev Lett*. 132(14):148401.

21 Wohlert J, Den Otter WK, Edholm O, Briels WJ. 2006. Free energy of a trans-membrane pore calculated from atomistic molecular dynamics simulations. *J Chem Phys*. 124(15):154905.

22 Bennett WD, Sapay N, Tieleman DP. 2014. Atomistic simulations of pore formation and closure in lipid bilayers. *Biophys J*. 106(1):210–219.

23 Evans E, Heinrich V, Ludwig F, Rawicz W. 2003. Dynamic tension spectroscopy and strength of biomembranes. *Biophys J*. 85(4):2342–2350.

24 Fernandez ML, Marshall G, Sagués F, Reigada R. 2010. Structural and kinetic molecular dynamics study of electroporation in cholesterol-containing bilayers. *J Phys Chem B*. 114(20): 6855–6865.

25 Kramar P, Miklavčič D. 2022. Effect of the cholesterol on electroporation of planar lipid bilayer. *Bioelectrochemistry*. 144:108004.

26 Lira RB, Leomil FS, Melo RJ, Riske KA, Dimova R. 2021. To close or to collapse: the role of charges on membrane stability upon pore formation. *Adv Sci*. 8(11):2004068.

27 Böckmann RA, De Groot BL, Kakorin S, Neumann E, Grubmüller H. 2008. Kinetics, statistics, and energetics of lipid membrane electroporation studied by molecular dynamics simulations. *Biophys J.* 95(4):1837–1850.

28 Gurtovenko AA, Vattulainen I. 2005. Pore formation coupled to ion transport through lipid membranes as induced by transmembrane ionic charge imbalance: atomistic molecular dynamics study. *J Am Chem Soc.* 127(50):17570–17571.

29 Tarek M. 2005. Membrane electroporation: a molecular dynamics simulation. *Biophys J.* 88(6):4045–4053.

30 Tieleman DP. 2004. The molecular basis of electroporation. *BMC Biochem.* 5(1):1–12.

31 Ting CL, Awasthi N, Müller M, Hub JS. 2018. Metastable prepores in tension-free lipid bilayers. *Biophys Rev Lett.* 120(12):128103.

32 Ziegler MJ, Vernier PT. 2008. Interface water dynamics and porating electric fields for phospholipid bilayers. *J Phys Chem B.* 112(43):13588–13596.

33 Piggot TJ, Holdbrook DA, Khalid S. 2011. Electroporation of the E. coli and S. aureus membranes: molecular dynamics simulations of complex bacterial membranes. *J Phys Chem B.* 115(45): 13381–13388.

34 Rems L, et al. 2022. Identification of electroporation sites in the complex lipid organization of the plasma membrane. *Elife.* 11: e74773.

35 Lorent JH, et al. 2020. Plasma membranes are asymmetric in lipid unsaturation, packing and protein shape. *Nat Chem Biol.* 16(6): 644–652.

36 Pogozheva ID, et al. 2022. Comparative molecular dynamics simulation studies of realistic eukaryotic, prokaryotic, and archaeal membranes. *J Chem Inf Comput Sci.* 62(4):1036–1051.

37 Reinhard J, et al. 2024. Memprep, a new technology for isolating organellar membranes provides fingerprints of lipid bilayer stress. *EMBO J.* 43(8):1653–1685.

38 Pluhackova K, Horner A. 2021. Native-like membrane models of E. coli polar lipid extract shed light on the importance of lipid composition complexity. *BMC Biol.* 19(1):1–22.

39 Hub JS. 2021. Joint reaction coordinate for computing the free-energy landscape of pore nucleation and pore expansion in lipid membranes. *J Chem Theory Comput.* 17(2):1229–1239.

40 Hub JS, Awasthi N. 2017. Probing a continuous polar defect: a reaction coordinate for pore formation in lipid membranes. *J Chem Theory Comput.* 13(5):2352–2366.

41 Hamm M, Kozlov M. 2000. Elastic energy of tilt and bending of fluid membranes. *Eur Phys J E.* 3(4):323–335.

42 Helfrich W. 1973. Elastic properties of lipid bilayers: theory and possible experiments. *Z Naturforsch C J Biosci.* 28(11-12):693–703.

43 Doktorova M, et al. 2023. Cell membranes sustain phospholipid imbalance via cholesterol asymmetry. bioRxiv pages 2023–07. https://doi.org/10.1101/2023.07.30.551157, preprint: not peer reviewed.

44 Strahl H, Errington J. 2017. Bacterial membranes: structure, domains, and function. *Annu Rev Microbiol.* 71(1):519–538.

45 Beltrán-Heredia E, et al. 2019. Membrane curvature induces cardiolipin sorting. *Commun Biol.* 2(1):225.

46 Litster J. 1975. Stability of lipid bilayers and red blood cell membranes. *Phys Lett A.* 53(3):193–194.

47 Taupin C, Dvolaitzky M, Sauterey C. 1975. Osmotic pressure-induced pores in phospholipid vesicles. *Biochemistry.* 14(21):4771–4775.

48 Sun J, Rutherford ST, Silhavy TJ, Huang KC. 2022. Physical properties of the bacterial outer membrane. *Nat Rev Microbiol.* 20(4): 236–248.

49 Schaefer SL, Hummer G. 2022. Sublytic gasdermin-d pores captured in atomistic molecular simulations. *Elife.* 11:e81432.

50 Awasthi N, et al. 2019. Molecular mechanism of polycation-induced pore formation in biomembranes. *ACS Biomater Sci Eng.* 5(2):780–794.

51 Ulmschneider JP, Ulmschneider MB. 2018. Molecular dynamics simulations are redefining our view of peptides interacting with biological membranes. *Acc Chem Res.* 51(5):1106–1116.

52 Verbeek SF, et al. 2021. How arginine derivatives alter the stability of lipid membranes: dissecting the roles of side chains, backbone and termini. *Eur Biophys J.* 50(2):127–142.

53 Kasparyan G, Poojari C, Róg T, Hub JS. 2020. Cooperative effects of an antifungal moiety and DMSO on pore formation over lipid membranes revealed by free energy calculations. *J Phys Chem B.* 124(40):8811–8821.

54 Poojari CS, Scherer KC, Hub JS. 2021. Free energies of membrane stalk formation from a lipidomics perspective. *Nat Commun.* 12(1):6594.

55 Mehnert T, Jacob K, Bittman R, Beyer K. 2006. Structure and lipid interaction of N-palmitoylsphingomyelin in bilayer membranes as revealed by 2H-NMR spectroscopy. *Biophys J.* 90(3): 939–946.

56 Niemelä P, Hyvönen MT, Vattulainen I. 2004. Structure and dynamics of sphingomyelin bilayer: insight gained through systematic comparison to phosphatidylcholine. *Biophys J.* 87(5): 2976–2989.

57 Israelachvili JN. *Intermolecular and surface forces* Academic Press, 2011.

58 West A, Ma K, Chung JL, Kindt JT. 2013. Simulation studies of structure and edge tension of lipid bilayer edges: effects of tail structure and force-field. *J Phys Chem A.* 117(32):7114–7123.

59 Sáenz JP, et al. 2015. Hopanoids as functional analogues of cholesterol in bacterial membranes. *PNAS.* 112(38):11971–11976.

60 Rawicz W, Olbrich KC, McIntosh T, Needham D, Evans E. 2000. Effect of chain length and unsaturation on elasticity of lipid bilayers. *Biophys J.* 79(1):328–339.

61 Szleifer I, Kramer D, Ben-Shaul A, Gelbart WM, Safran SA. 1990. Molecular theory of curvature elasticity in surfactant films. *J Chem Phys.* 92(11):6800–6817.

62 Israelachvili JN, Marčelja S, Horn RG. 1980. Physical principles of membrane organization. *Q Rev Biophys.* 13(2):121–200.

63 Fuller N, Rand R. 2001. The influence of lysolipids on the spontaneous curvature and bending elasticity of phospholipid membranes. *Biophys J.* 81(1):243–254.

64 Hu Q, et al. 2005. Simulations of transient membrane behavior in cells subjected to a high-intensity ultrashort electric pulse. *Phys Rev E.* 71(3):031914.

65 Vernier PT, et al. 2006. Nanopore formation and phosphatidylserine externalization in a phospholipid bilayer at high transmembrane potential. *J Am Chem Soc.* 128(19):6288–6289.

66 Allolio C, Harries D. 2021. Calcium ions promote membrane fusion by forming negative-curvature inducing clusters on specific anionic lipids. *ACS Nano.* 15(8):12880–12887.

67 Konar S, Arif H, Allolio C. 2023. Mitochondrial membrane model: lipids, elastic properties and the changing curvature of cardiolipin. *Biophys J.* 122(21):4274–4287.

68 Venable RM, Brown FL, Pastor RW. 2015. Mechanical properties of lipid bilayers from molecular dynamics simulation. *Chem Phys Lipids.* 192:60–74.

69 Rand RP, Fuller NL, Gruner SM, Parsegian VA. 1990. Membrane curvature, lipid segregation, and structural transitions for phospholipids under dual-solvent stress. *Biochemistry.* 29(1): 76–87.

70 Sodt AJ, Venable RM, Lyman E, Pastor RW. 2016. Nonadditive compositional curvature energetics of lipid bilayers. *Phys Rev Lett*. 117(13):138104.

71 Chernomordik L, *et al*. 1985. The shape of lipid molecules and monolayer membrane fusion. *Biochim Biophys Acta Biomembr*. 812(3):643–655.

72 Karatekin E, *et al*. 2003. Cascades of transient pores in giant vesicles: line tension and transport. *Biophys J*. 84(3):1734–1749.

73 Portet T, Dimova R. 2010. A new method for measuring edge tensions and stability of lipid bilayers: effect of membrane composition. *Biophys J*. 99(10):3264–3273.

74 Tazawa K, Yamazaki M. 2023. Effect of monolayer spontaneous curvature on constant tension-induced pore formation in lipid bilayers. *J Chem Phys*. 158(8):081101.

75 Zhelev DV, Needham D. 1993. Tension-stabilized pores in giant vesicles: determination of pore size and pore line tension. *Biochim Biophys Acta Biomembr*. 1147(1):89–104.

76 Kramar P, Miklavcic D, Lebar AM. 2009. A system for the determination of planar lipid bilayer breakdown voltage and its applications. *IIEEE Trans Nanobiosci*. 8(2):132–138.

77 Levine ZA, Vernier PT. 2012. Calcium and phosphatidylserine inhibit lipid electropore formation and reduce pore lifetime. *J Membr Biol*. 245(10):599–610.

78 Griffiths G, *et al*. 1989. The dynamic nature of the golgi complex. *J Cell Biol*. 108(2):277–297.

79 Lessen HJ, Sapp KC, Beaven AH, Ashkar R, Sodt AJ. 2022. Molecular mechanisms of spontaneous curvature and softening in complex lipid bilayer mixtures. *Biophys J*. 121(17): 3188–3199.

80 Pöhnl M, Trollmann MF, Böckmann RA. 2023. Nonuniversal impact of cholesterol on membranes mobility, curvature sensing and elasticity. *Nat Commun*. 14(1):8038.

81 Abraham MJ, *et al*. 2015. GROMACS: high performance molecular simulations through multi-level parallelism from laptops to supercomputers. *SoftwareX*. 1-2:19–25.

82 Awasthi N, Hub JS. Free-energy calculations of pore formation in lipid membranes. In: Berkowitz ML, editor, *Biomembrane simulations: computational studies of biological membranes* CRC Press, 2019. p. 109–124.

83 Klauda JB, Monje V, Kim T, Im W. 2012. Improving the CHARMM force field for polyunsaturated fatty acid chains. *J Phys Chem B*. 116(31):9424–9431.

84 Klauda JB, *et al*. 2010. Update of the CHARMM all-atom additive force field for lipids: validation on six lipid types. *J Phys Chem B*. 114(23):7830–7843.

85 Lim JB, Rogaski B, Klauda JB. 2012. Update of the cholesterol force field parameters in CHARMM. *J Phys Chem B*. 116(1): 203–210.

86 Venable RM, *et al*. 2014. CHARMM all-atom additive force field for sphingomyelin: elucidation of hydrogen bonding and of positive curvature. *Biophys J*. 107(1):134–145.

87 West A, *et al*. 2020. How do ethanolamine plasmalogens contribute to order and structure of neurological membranes? *J Phys Chem B*. 124(5):828–839.

88 Allolio C, Haluts A, Harries D. 2018. A local instantaneous surface method for extracting membrane elastic moduli from simulation: comparison with other strategies. *Chem Phys*. 514: 31–43.

89 Balusek C, *et al*. 2019. Accelerating membrane simulations with hydrogen mass repartitioning. *J Chem Theory Comput*. 15(8): 4673–4686.

90 Bernetti M, Bussi G. 2020. Pressure control using stochastic cell rescaling. *J Chem Phys*. 153(11):114107.

91 Bjelkmar P, Larsson P, Cuendet MA, Hess B, Lindahl E. 2010. Implementation of the CHARMM force field in gromacs: analysis of protein stability effects from correction maps, virtual interaction sites, and water models. *J Chem Theory Comput*. 6(2):459–466.

92 Essmann U, *et al*. 1995. A smooth particle mesh Ewald method. *J Chem Phys*. 103(19):8577–8593.

93 Goetz R, Lipowsky R. 1998. Computer simulations of bilayer membranes: self-assembly and interfacial tension. *J Chem Phys*. 108(17):7397–7409.

94 Hess B. 2007. P-LINCS: a parallel linear constraint solver for molecular simulation. *J Chem Theory Comput*. 4(1):116–122.

95 Hoover WG. 1985. Canonical dynamics: equilibrium phase-space distributions. *Phys Rev A*. 31(3):1695–1697.

96 Hub JS, De Groot BL, van der Spoel D. 2010. g_wham - a free weighted histogram analysis implementation including robust error and autocorrelation estimates. *J Chem Theory Comput*. 6(12):3713–3720.

97 Jo S, Kim T, Iyer VG, Im W. 2008. CHARMM-GUI: a web-based graphical user interface for CHARMM. *J Comput Chem*. 29(11): 1859–1865.

98 Jo S, Lim JB, Klauda JB, Im W. 2009. CHARMM-GUI membrane builder for mixed bilayers and its application to yeast membranes. *Biophys J*. 97(1):50–58.

99 Jorgensen WL, Chandrasekhar J, Madura JD, Impey RW, Klein ML. 1983. Comparison of simple potential functions for simulating liquid water. *J Chem Phys*. 79(2):926–935.

100 Knight CJ, Hub JS. 2015. MemGen: a general web server for the setup of lipid membrane simulation systems. *Bioinformatics*. 31(17):2897–2899.

101 Kumar S, Bouzida D, Swendsen R, Kollman P, Rosenberg J. 1992. The weighted histogram analysis method for free-energy calculations on biomolecules. I. The method. *J Comput Chem*. 13(8): 1011–1021.

102 Miyamoto S, Kollman PA. 1992. Settle: an analytical version of the shake and rattle algorithm for rigid water models. *J Comput Chem*. 13(8):952–962.

103 Nosé S. 1984. A molecular dynamics method for simulations in the canonical ensemble. *Mol Phys*. 52(2):255–268.

104 Parrinello M, Rahman A. 1980. Crystal structure and pair potentials: a molecular-dynamics study. *Phys Rev Lett*. 45(14): 1196–1199.

105 Schofield P, Henderson JR. 1982. Statistical mechanics of inhomogeneous fluids. *Proc R Soc Lond A*. 379(1776):231–246.

106 Sega M, Fábián B, Jedlovszky P. 2016. Pressure profile calculation with mesh Ewald methods. *J Chem Theory Comput*. 12(9): 4509–4515.

107 Torrie GM, Valleau JP. 1974. Monte Carlo free energy estimates using non-Boltzmann sampling: application to the sub-critical Lennard-Jones fluid. *Chem Phys Lett*. 28(4):578–581.

108 Starke L, Allolio C, Hub JS. 2024. Pore formation in complex biological membranes: torn between evolutionary needs. bioRxiv pages 2024–05. https://doi.org/10.1101/2024.05.06.592649, preprint: not peer reviewed.